Longitudinal phase space diagnostics with a nonmovable corrugated passive wakefield streaker

Philipp Dijkstal[*], Weilun Qin, and Sergey Tomin[†]

Deutsches Elektronen-Synchrotron DESY, Notkestr. 85, 22607 Hamburg, Germany

Time-resolved diagnostics at free-electron laser (FEL) facilities, in particular electron beam longitudinal phase space (LPS) and FEL power profile measurements, provide information highly valuable for users, machine development studies, and beam setup. We investigate the slice energy resolution of passive streaker setups, in particular the effect of an energy chirp on the measured slice energy spread. Downstream of the hard x-ray SASE2 beamline at the European XFEL, these measurements are enabled by a single-plate nonmovable passive wakefield streaker, essentially a rectangular corrugated plate placed inside a vacuum chamber. We show measurements with a time resolution down to a few femtoseconds and an energy resolution down to a few MeVs.

I. INTRODUCTION

Electron beam longitudinal phase space (LPS) measurements performed after free-electron laser (FEL) [1,2] undulator beamlines provide information that is highly relevant for FEL operation and machine development, in particular the beam current profile, the energy chirp (the change of the slice mean energy along the bunch), and the slice energy spread. High beam currents are important for FEL performance and efficiency. Moreover, knowledge of the current profile is required to calculate the undulator wakefields. Knowledge of the energy chirp and the undulator wakefields allows to predict the optimal undulator taper profile [3]. A strong chirp imposes a relation between time and central frequency of the FEL pulse, interesting for some applications [4], and increases the FEL bandwidth. While the vast majority of users at FEL facilities request a minimal bandwidth, others benefit from maximal bandwidth [5]. A small slice energy spread is fundamental for high-gain FELs [6,7], and measurements are helpful for optimizations such as finding the optimal laser heater [8] working point. Additionally, LPS measurements are the basis for indirect FEL pulse duration and power profile measurements [9–11], which are among the most important FEL parameters. In particular, many users of x-ray FEL facilities request short pulses [12–14].

The LPS is typically measured with transversely deflecting rf structures (TDS) that impose a linear correlation between time and transverse beam coordinates [9,10,15,16], and a transverse profile imager [17] (beam screen) at a dispersive location. In recent years, passive wakefield streakers (PS) have emerged as an alternative to TDS [11,18–20] and are now employed for time-resolved measurements of multi-GeV electron beams at the SwissFEL [21] Aramis beamline and the European XFEL [22] (EuXFEL) SASE2 beamline. In a PS, the bunch receives a time-dependent transverse kick similar to a TDS. There are two PS variants, which generate wakefields either from corrugated [23] or dielectric [18] surfaces. Compared to a TDS, a PS has far lower construction and operating costs. Furthermore, wakefield streaking is inherently synchronized to the beam arrival time. The main disadvantage of PS is the nonlinearity of wakefield streaking, which causes a varying time resolution along the bunch. In particular, the head of the beam is not resolved. Moreover, complex analysis algorithms are required.

LPS diagnostics ideally have time and energy resolutions better than the values to be measured. The final bunch durations at hard x-ray FEL user facilities are on the order of a few tens of fs, while the FEL pulses can be shorter: sub-fs durations have been achieved [24,25]. At different FEL facilities, the beam slice energy spread at the beginning of the undulator section was measured at the 100 keV level [26] (FERMI [27]) and the MeV level [28] (SwissFEL). The high-gain FEL instability inside the undulator section can increase the slice energy spread to the 10 MeV level [10,29]. Therefore, LPS measurements of the nonlasing beam have higher requirements on the energy resolution compared to measurements of the lasing beam at optimized

---

performance. Previous publications on PS diagnostics focus on lattice design for an optimal time resolution [30], current profile measurements [18,19], and FEL power profile measurements [11], less so on stand-alone LPS measurements. We show in this paper that the energy resolution in LPS measurements based on electron streaking is slice dependent and that the energy chirp has an impact on the observed slice energy spread. The varying time resolution of PS diagnostics exacerbates this effect. Here we provide the theoretical understanding necessary to interpret LPS measurements.

Double-sided movable corrugated PS is used for diagnostics purposes at SwissFEL [31] (and at relatively low beam energy at the PAL-XFEL injector test facility [19,32]). The PS at EuXFEL has a simpler design with a single, nonmovable corrugated plate, which is advantageous in terms of vacuum safety and cost-efficiency. It has previously been successfully employed to observe qualitative features of the FEL pulse [20] and for slice energy spread measurements without time calibration [33]. In this paper, we show its first time-resolved measurements of important properties such as the electron beam energy chirp and the FEL pulse duration.

An analytical wakefield model [34,35] is the basis for our analysis. It contains the transverse dipole and quadrupole components and the longitudinal component up to first order. The transverse dipole component deflects the beam toward the structure. The transverse quadrupole component has a defocusing effect in the streaking direction and a focusing effect in the other transverse direction. The longitudinal component causes a slice energy loss. All effects are weakest at the head and grow stronger along the bunch.

In this paper, we first describe the experimental setup at EuXFEL in Sec. II. Then we present the expected time and slice energy resolution of a PS diagnostics setup in Sec. III. Afterward, we discuss LPS and FEL power profile measurements in Sec. IV.

II. EXPERIMENTAL SETUP

The European XFEL is a high repetition rate x-ray FEL user facility powered by a superconducting linac [22]. It accelerates 10 macropulses per second, each of which contains up to 2700 electron bunches. The final beam energy is up to 17.5 GeV, the nominal bunch charge is 250 pC, and the normalized transverse emittance is less than 0.6 μm. The bunches are distributed among three undulator beamlines, where they generate intense x-ray FEL radiation with tunable photon energies between approximately 0.25 and 25 keV. The FEL pulses are used in the experimental end stations for research of ultrafast phenomena in matter at the atomic scale. Beam optics are regularly measured and matched in the injector section [36]. The CRISP THz spectrometer noninvasively measures the current profile at the end of the linac section [37],
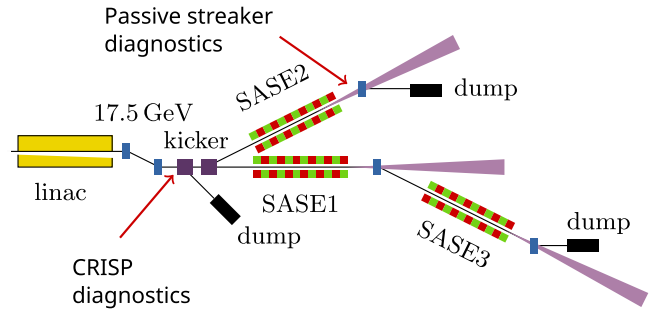

FIG. 1. Layout of EuXFEL after the final compression stage (taken from [37], modified).

with a time resolution that can generally be estimated at 8 fs and averages over 16 bunches. X-ray gas monitors measure the FEL pulse energy with an uncertainty of less than 10% [38]. Figure 1 shows the relevant part of the EuXFEL layout.

The EuXFEL passive streaker, designed at DESY, is essentially a vacuum chamber that contains a 5 m long rectangular corrugated plate. Steering dipoles can move the beam closer to the plate and thereby control the streaking magnitude. A larger orbit bump results in a smaller distance d between beam and plate, and in stronger wakefields. The first dipole in the arc after SASE2 serves as an energy spectrometer in the horizontal plane. Several measurement optics with optimized time resolution and with different dispersion values at the beam screen in the arc can be set [20]. In general, a beam screen can only resolve one bunch per macropulse. With the PS in operation, beam losses further limit the beam repetition rate to one bunch in every third macropulse. For measurements of the nonlasing beam, we use a steering dipole to introduce horizontal betatron oscillations within SASE2 and thereby disable the FEL process. Figure 2 shows the PS diagnostics setup after the SASE2 beamline and a schematic of the corrugation geometry. Table I contains important parameters of the diagnostics setup.
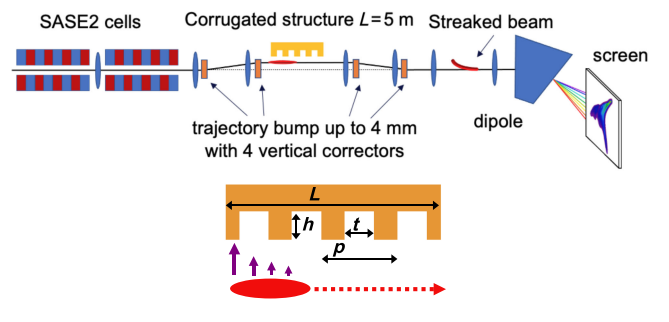

FIG. 2. Top: layout of the diagnostic beamline for LPS measurements after the SASE2 undulator beamline. Bottom: geometry of the corrugated plate. The growing wakefield forces along the bunch are indicated by purple arrows.

TABLE I. The corrugation parameters according to the sketch in Fig. 2 bottom left, and the relevant beam optics and transport lattice parameters for the measurements shown in this paper [20].

Corrugation geometry	Depth, h	0.5 mm
	Gap, t	0.25 mm
	Period, p	0.5 mm
	Width, w	12 mm
	Length, L	5 m
Beam optics at PS	β_x, α_x	34.5 m, 1.0
	β_y, α_y	54.2 m, −1.9
Transport lattice	Dispersion	30 cm
	R_{34}	−40 m
	$\Delta\mu_y$	281°
Beam optics at screen	β_x, β_y	4.9 m, 30 m

III. MEASUREMENT RESOLUTION

In the following, we first recall the time resolution theory for passive streakers and find an expression for the time-dependent energy resolution for LPS measurements based on electron streaking. Then, we confirm these results with ideal beam macroparticle simulations.

A. Expressions for time and energy resolution

While we want to measure the time and energy (t and E) distribution in an LPS measurement, we can only see the transverse (y and x) distribution on a beam screen. For this reason, we impose correlations between t and y and between x and E. Yet as a consequence of the natural beam size and the complex structure wakefield effects, particles with different t or E coordinates can have the same y or x coordinates on the screen and thus the resolving power of the diagnostics is limited. The time and energy resolution specify the smallest temporal and energetic features of the beam that can be measured. Lower resolution values are preferable. We emphasize that the main cause of the resolution is beam dynamics, not the camera pixel size or the finite screen resolution σ_R. In our case, σ_R is better than 10 μm [17], similar to or less than the natural rms beam sizes at the screen position. Therefore, even ideal hardware ($\sigma_R = 0$) and infinitesimally fine image slicing would not significantly improve the measurement resolution.

The rms time resolution r_t of a PS measurement setup with transverse dipole and quadrupole wakefields components is [30]:

$$r_t(t) = \frac{\sigma_y(t)}{|\mathrm{d}y(t)/\mathrm{d}t|}, \tag{1}$$

with the time-resolved slice beam size at the screen in streaking direction $\sigma_y(t)$ and the streaking term at the screen $\mathrm{d}y(t)/\mathrm{d}t$. The screen resolution σ_R adds in

quadrature to the beam size, but we omit it for clarity. The streaking term is zero at the head of the beam and progressively increases along the bunch. Therefore, r_t diverges at the head. The defocusing quadrupole wakefields are negligible at the head but increase toward the tail at a faster rate than the dipole wakefields responsible for the streaking. Reference [30] contains expressions of σ_y as a function of transverse emittance and Twiss parameters at the PS, of quadrupole wakefield strength, and of the transport lattice between structure and screen.

In the following, we consider the rms energy resolution r_E and the interplay with the time resolution. The energy resolution r_E of a dipole spectrometer setup is typically given as [9]

$$r_E = E_0 \frac{\sigma_{x0}}{|D|}, \tag{2}$$

with the average beam energy E_0, the dispersion D, and the slice beam size at the screen σ_{x0} (in the absence of dispersion). For TDS setups, it can be reasonable to assume that σ_{x0} is the same for each slice. Conversely, the quadrupole wakefields in a PS setup act as a quadrupole magnet with time-dependent strength and give a slice optics mismatch along the bunch [39]. However, we find that Eq. (2) does not explain the large slice energy spread we measure with a PS:

$$\sigma_{Em}(t) = E_0 \frac{\sigma_x(t)}{|D|}, \tag{3}$$

with $\sigma_x(t)$ the dispersive beam size measured on the screen. We introduce the slice energy resolution r_E^* to quantify the differences between measured (σ_{Em}) and true initial (σ_E) energy spread:

$$r_E^*(t) \equiv \sqrt{\sigma_{Em}^2(t) - \sigma_E^2(t)}, \tag{4}$$

and identify two effects that increase σ_{Em} in addition to the natural beam size effect.

First, any additional slice energy spread $\Delta\sigma_E$ induced by the PS (if placed before the energy spectrometer) contributes to σ_{Em}. The corresponding analytical expression is absent from Refs. [34,35] but is easily calculated from the information therein (Appendix A). We note that also TDS increases the slice energy spread, which is corrected in high-resolution energy spread measurements [16,28,40,41].

Second, due to the finite time resolution, particles from different time slices end up at the same y position on the screen. If these time slices have different mean energies, the measured energy spread (of all particles with the same y coordinate) is larger than the true energy spread (of all particles with the same t coordinate). We call this effect a spillover of time to energy resolution. Consistent with this description, in measurements of beams with quadratic

energy chirp, the minimum slice energy spread is found at the time slice with zero chirp [41]. In Appendix B, we analytically verify the effect for a simplified case.

Neglecting correlations between transverse and energy coordinates imposed by higher-order wakefields, and assuming a slowly varying current profile, the total slice energy resolution $r_E^*(t)$ is the quadratic sum of the three effects:

$$r_E^*(t) = \sqrt{\left(\frac{E_0\sigma_{x0}(t)}{D}\right)^2 + \Delta\sigma_E^2(t) + \left(r_t(t)\frac{dE(t)}{dt}\right)^2}. \quad (5)$$

The first term (proportional to σ_{x0}) varies slightly along the beam due to the focusing quadrupole wakefield effect. The second term ($\Delta\sigma_E$) steadily increases along the bunch. The third term is proportional to the energy chirp $dE(t)/dt$ and can have any behavior. We note that in most situations where the LPS is measured, it would be nonsensical to beforehand alter the LPS for minimal chirp and optimal r_E^*. Only in some cases, this is feasible, such as for the measurements of the quantum diffusion effect previously performed at EuXFEL with the PS [33].

B. Simulated LPS measurement

We illustrate the resolution effects described above by simulating LPS measurements based on electron streaking. We assume that the current profile and the distance between beam and corrugated plate, and thus the PS wakefield potentials, are known. First, we generate a 6D macro-particle distribution describing the incoming electron beam. For simplicity, we choose a rectangular 5 kA current profile. Inspired by measurements shown later, we set the linear energy chirp to -1.5 MeV/fs. Moreover, the initial beam has zero slice energy spread, thus we have the condition $\sigma_{Em} = r_E^*$. Other parameters are 14 GeV mean beam energy, 250 pC bunch charge, the transverse optics at the PS location listed in Table I, and a normalized transverse emittance of 0.6 μm. For the time streaking effect, we consider two variants. First, linear streaking is essentially

an ideal TDS setup neglecting its side effects on the beam energy [16] (*Linear*). Second, the PS case with all wakefield components enabled (*PS*). In both cases, we choose the streaking strength such that the total extent of the beam along the streaked coordinate y is approximately 1 mm. For the *PS* case. we use $d = 600$ μm. Finally, we track the particle distribution to the screen using the linear transport optics described in Table I. Figure 3 shows the initial distribution in t and E coordinates (a), and the distributions in y and x coordinates at the screen for the two cases (b)–(c).

In the analysis, we first calculate the time resolution by directly evaluating Eq. (1) from the y macroparticle coordinates at the screen and the initial t coordinates. We note that the reconstruction of the time coordinates refers to the beam at the PS and not at the screen, even though longitudinal dispersion introduced by the spectrometer dipole alters the current profile between these two positions. As expected, we obtain a constant r_t for the *Linear* case, and a diverging r_t at the head of the beam for the *PS* case [Fig. 4(a)]. For *PS*, we obtain a minimal r_t below 2 fs at the center.

Next, we imitate a measurement of the slice mean energy E_m and the slice energy spread σ_{Em} by projecting the 6D particle distribution to just x and y and slicing it along y. In the trivial linear streaking case, we obtain the t axis from a division of the y axis by the streaking term $\Delta y/\Delta t$. In the *PS* case, we retrieve the t axis from the transverse dipole wakefield potential. We calculate E_m and σ_{Em} from a center of mass and rms calculation and evaluate r_E^*. Figures 4(b)–4(d) displays the results of our analysis. Plot (b) shows the difference between the true (black) and measured (colors) slice mean energy deviation. There is excellent agreement in the *Linear* case, whereas the *PS* case includes the energy loss from the longitudinal wakefields and thus gives a different result. This underscores the importance of correcting the slice mean energy loss from the longitudinal structure wakefields. Knowledge of the current profile and of d is sufficient to calculate the main effect. We find the energy loss correction term described in Appendix A to be negligible.
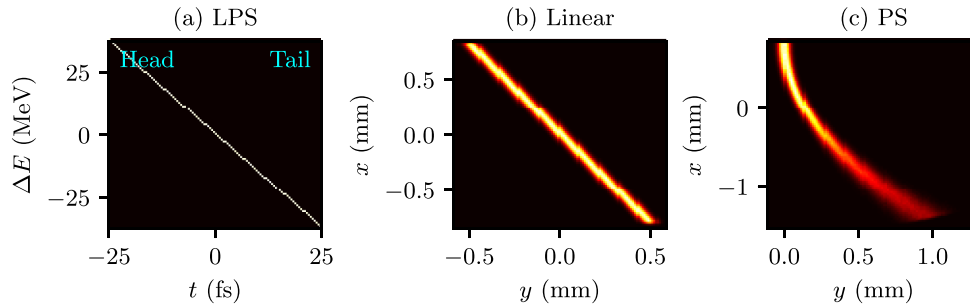

FIG. 3.   Ideal beam simulations of LPS measurements based on electron streaking. (a) Initially generated beam with zero energy spread. (b),(c) Simulated transverse distribution at the screen for two cases: linear streaking (b), and wakefield streaking (c). We display the y coordinate in the horizontal direction for consistency with the conventional display of LPS measurements.
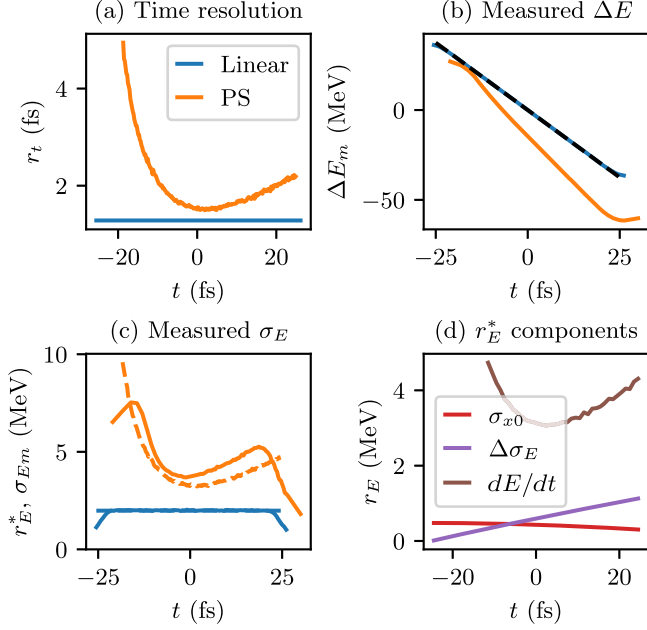
FIG. 4. Slice mean energy and energy spread analysis of the simulated LPS of Fig. 3. (a) Time resolution of the measurements. (b) Reconstructed slice mean energy ΔE_m (colors) and true ΔE_m (dashed black). (c) Reconstructed slice energy spread σ_{Em} in solid, and slice energy resolution r_E^* in dashed and matching colors. Colors in (b),(c) refer to the legend of plot (a). (d) The three components of r_E^* as in Eq. (5) for the PS case.

In Fig. 4(c), we show the numerically evaluated slice energy spread σ_{Em} (solid) compared to the prediction r_E^* (dashed). For the *Linear* case, we find exact agreement. For the *PS* case, there is good agreement, with a minimal r_E^* between 3.5 and 4 MeV at the center of the bunch. However, the actual measured energy spread is slightly underestimated by r_E^*. Plot (d) displays the three components of r_E^* for the *PS* case (see Eq. (5)). The contribution of the natural beam size (σ_{x0}) is on the order of 0.5 MeV and decreases toward the tail of the beam due to the focusing quadrupole wakefield effect. The energy spread induced by the PS ($\Delta\sigma_E$) has an approximately linear growth along the bunch and reaches up to 1 MeV at the tail. The energy chirp term is the by far largest contribution, with a minimum of around 3 MeV at the beam center. The simulations show that the expected slice energy resolution of the energy-chirped beam is on the order of several MeV, higher than the energy spread expected for the nonlasing beam at an FEL facility and less than what is expected for the lasing beam.

In Appendix C, we compare the macroparticle tracking functionality of our analysis software [29] and the OCELOT code [42]. We find good agreement between the codes for the values of d we typically set, which includes the measurements and simulations shown in this paper. Only for smaller d, the more precise but also more time-consuming wakefield implementation of OCELOT is preferable.

IV. MEASUREMENTS AT EUXFEL

In the following pages, we analyze various measurements performed with the PS after SASE2. We start with a single LPS measurement (with the FEL disabled) to illustrate the procedure, in particular the time calibration. Afterward, we analyze three LPS measurements of the same beam conditions under variation of d. Finally, we also demonstrate an example FEL power profile measurement.

A. Time calibration and LPS measurement

In our analysis procedures [11,29], we first determine d through an iterative process. In essence, we record the current profile measured by CRISP and the vertical beam center of mass on the screen before and after the streaking conditions are set. In PS macroparticle tracking simulations using the measured current profile, we vary d until we match the center of mass shift recorded earlier. Then, we calculate the impact of the wakefield kick at the position of the beam screen, using the transverse dipole wakefield potential and the R_{34} beam transport matrix element. This lets us convert the vertical image axis to time. We ensure that the calibration is reasonable by comparing the shape and rms duration of the current profile as reconstructed from the transverse beam profile (using the algorithm from Ref. [11]) to the CRISP measurement. Finally, we convert the horizontal image axis to energy with the known dispersion value. We note that the assumption of transverse beam optics does not affect the simulated center of mass deflection of the beam and thus also not the distance calibration procedure.

The calibration and LPS measurement procedure is demonstrated in Fig. 5. Plots (a),(b) show the recorded screen image and the CRISP profile, which serve as an input to the calibration procedure. Plots (c),(d) show the outcome of the particle tracking: the transverse projections on the screen (c), and the center of mass shift (d). We also find good agreement between the reconstructed and CRISP current profiles (b). The calibration curves obtained from the dipole wake potentials of the two current profiles are virtually identical (e). We use the calibration curve from the CRISP profile to convert the raw image to LPS (f).

B. Slice energy properties measured under variation of streaking strength

Earlier, we discussed the influence of the time resolution r_t on the slice energy resolution r_E^*, and the influence of the longitudinal wakefields on the slice mean energy. Both effects have a strong dependency on d. In the following, we analyze LPS measurements taken with different beam trajectories inside the PS.

Figures 6(a)–6(c) shows three consecutive LPS measurements, between each of which we decreased the d set value by 100 μm. The calibrated d changes by 79 and 121 μm, giving differences between result and expectation
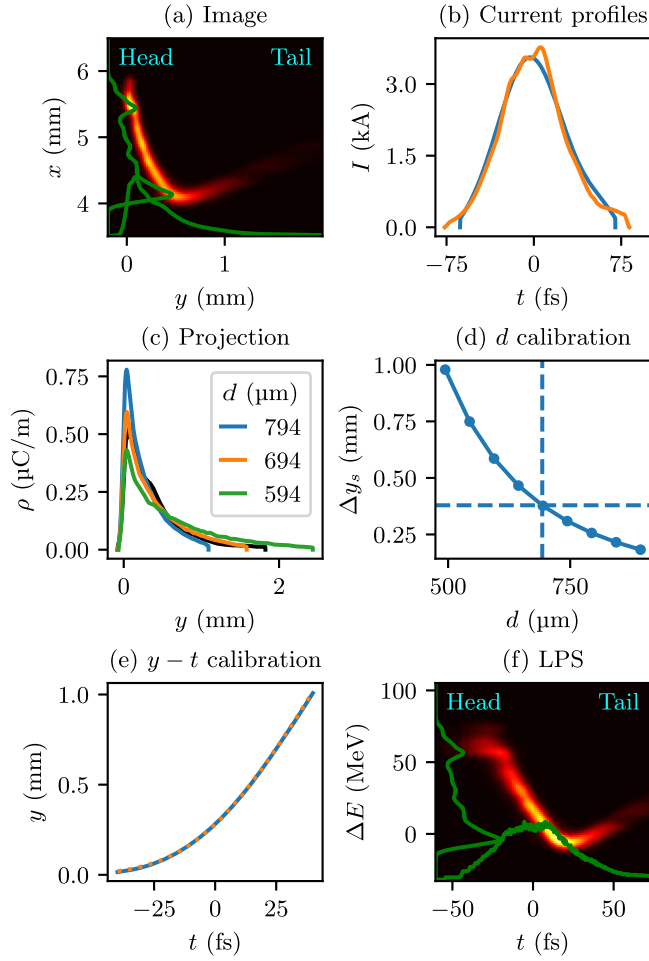
FIG. 5. LPS measurement including distance (d) calibration procedure. (a) Measured transverse projection of the streaked beam, again with the y coordinate in the horizontal direction for consistency. (b) CRISP (blue) and reconstructed (orange) current profiles. (c) Measured (black) and simulated (colors) streaked projections at the screen assuming three different d. (d) Simulated transverse center of mass shift. The dashed horizontal line indicates the measured shift. The dashed vertical line indicates the calibrated d of 694 μm. (e) Time calibration curves, using the current profiles from (b) as input (same colors). (f) Reconstructed LPS.

of ± 21 μm which we attribute to errors in the set trajectory. For a consistency check, we compare CRISP and reconstructed current profiles and find good agreement in each case (d). The effect of the microbunching instability [40] is clearly visible in the single-shot PS measurements, but not in the CRISP measurement that is averaged over several shots.

In Fig. 7, we analyze the slice mean energy. We limit the analysis to parts of the beam with a current over 1 kA, such that the results are less affected by noise. Plot (a) shows the uncorrected ΔE_m. At the head and center, for all d, we measure a negative energy chirp of -1.5 MeV/fs. Toward the tail, the chirp decreases and turns to positive values,
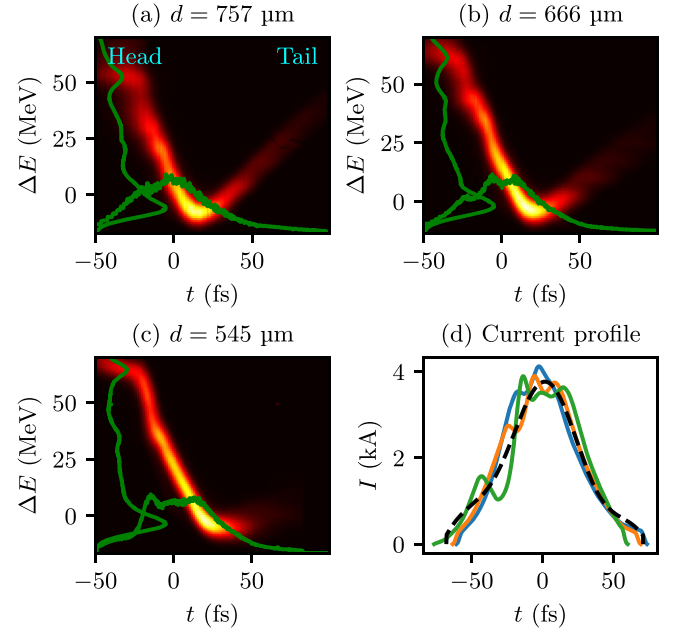

FIG. 6. (a)–(c) Three LPS measurements acquired under the same beam conditions but varying beam trajectory inside the PS. The calibrated d are listed in the titles. (d) Reconstructed current profiles from the PS (colors) and from CRISP (dashed).

although there are pronounced differences of up to 15 MeV between the three measurements. We calculate the expected wakefield energy loss based on the CRISP current profile and display the corrected slice energy values ΔE_c in (b). At the head and center, the energy chirp is reduced to about -1.2 MeV/fs. At the tail, differences between the measurements persist but are smaller in magnitude by about a factor of 2. The analysis indicates that we underestimate the slice energy loss imposed by the PS at the tail and thus cannot accurately measure the energy chirp there.

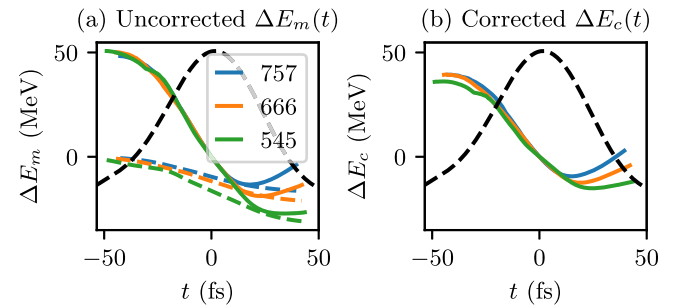In Fig. 8, we analyze the measurement resolution and the measured energy spread. We begin with r_t, which is

FIG. 7. Slice mean energy analysis for the LPS measured at different d as shown in Fig. 6. (a) Raw slice mean energy ΔE_m (solid). Estimated longitudinal wakefield contribution to ΔE_m. The legend indicates d in units of μm. (b) Corrected slice mean energy ΔE_c. In both plots, the CRISP current profile is overlaid in arbitrary units (dashed black), and the relative energy is shifted to zero at $t = 0$.
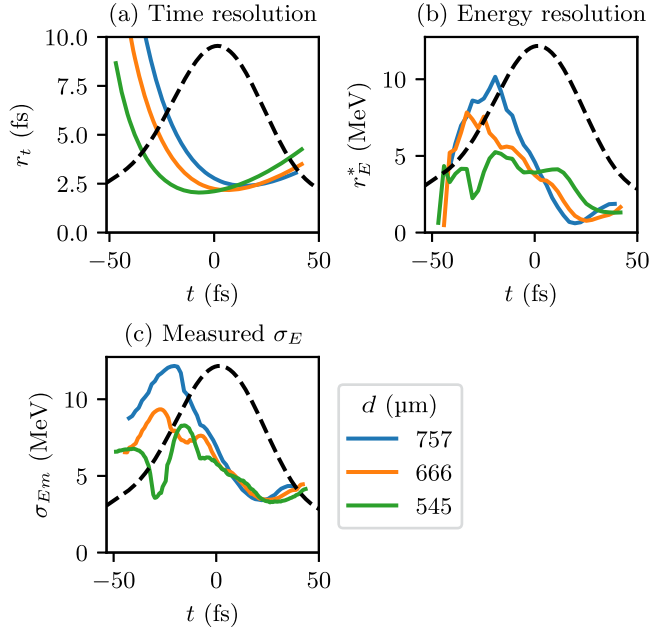
FIG. 8.   Slice energy spread and resolution analysis for the LPS measured at different d as shown in Fig. 6. (a), (b) Calculated time and slice energy resolution. (c) Measured slice energy spread. In all plots, the CRISP current profile is overlaid in arbitrary units (dashed black).

evaluated assuming design transverse optics (a). The minimum values of r_t are close to 2.5 fs for each d. Plot (b) shows r_E^* which we calculated using $\mathrm{d}E/\mathrm{d}t$ extracted from E_m shown in Fig. 7(a). Finally, we display σ_{Em} (c). The large differences between the three measurements indicate strong resolution effects and are expected considering the impact of d on r_t. Consistent with the resolution theory, the minimum energy spread (about 3.5 MeV in all cases) is observed for the slices without uncorrected energy chirp. The time coordinate of this slice changes with d because of the additional energy chirp imposed by the PS. The calculated r_E^* are generally similar in shape to the measured σ_{Em}. However, an evaluation of the true slice beam energy spread through subtraction of r_E^* [see Eq. (4)] would still yield implausibly large values, indicating that we underestimate r_E^*.

C. FEL power profile measurement

For an FEL power profile measurement, we combine the slice properties acquired at lasing-enabled and lasing-disabled beam orbit conditions in the undulator. The FEL power profile can be reconstructed using two methods [10]. First, through the slice mean energy loss caused by the FEL (P_Δ), and second, through the increase in slice energy spread σ_E caused by the FEL (P_σ), with

$$P_\sigma(t) \propto I^{2/3}(t)[\sigma_{E,\mathrm{on}}^2(t) - \sigma_{E,\mathrm{off}}^2(t)]. \tag{6}$$

We typically acquire 20 LPS measurements for each configuration, then use the average σ_E values to calculate the average P_σ, which we then normalize through the x-ray gas monitor pulse energy measurement. Afterward, we use the same normalization factor in combination with the single-shot $\sigma_{E,\mathrm{on}}$ and the average $\sigma_{E,\mathrm{off}}$ to obtain single-shot P_σ. An important feature of P_σ is that the impact of r_E^* cancels in case the vertical beam trajectory inside the PS is maintained for the two FEL configurations. We do not correct the LPS measurements for the incoming mean beam energy jitter (which would be possible) and neither for the energy chirp jitter (which would be difficult). Both jitters have a large impact on P_Δ and a small impact on P_σ. Thus, we only show P_σ in the following.

We performed an FEL power profile measurement with the same machine conditions as for the measurements presented earlier. The undulators were tuned to a resonant photon energy of 9 keV, and the average FEL pulse energy measured with the x-ray gas monitor was 300 µJ. The average calibrated d is 620 µm.

Figure 9 shows our results. The energy spread blowup caused by the FEL is clearly visible in the example LPS (a),(b). Fig. 9(c) show the measured slice energy spread values, which results in the power profiles in (d). Within the lasing part of the beam, $\sigma_{E,\mathrm{off}}$ (also an upper limit of r_E^*) is up to 7.5 MeV, while $\sigma_{E,\mathrm{on}}$ is up to 15 MeV,
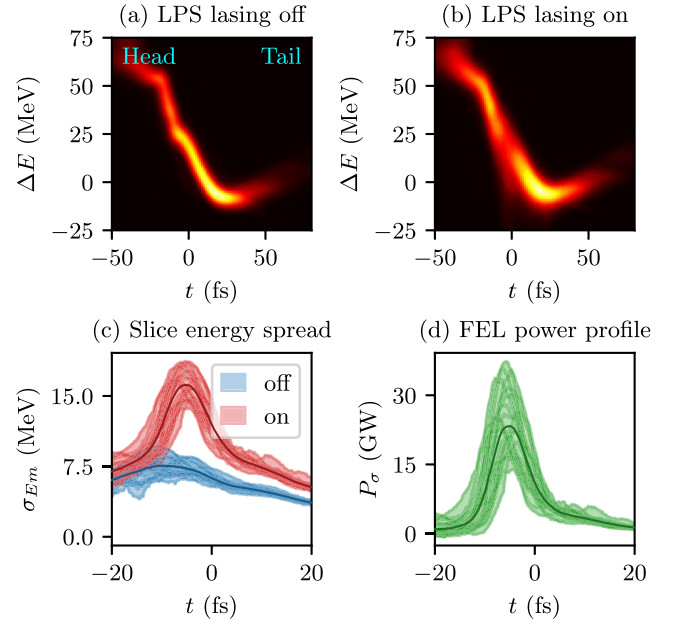

FIG. 9.   LPS measurements at lasing-disabled (a) and lasing-enabled (b) undulator configurations are combined for an FEL power profile measurement, (c) shows the σ_{Em} values for the two conditions, and (d) shows the FEL power profiles reconstructed from the increased energy spread when the FEL is enabled. The lightly colored lines show single-shot values, and the darkly colored lines the average value of 20 shots.

indicating a slice energy resolution sufficient for the FEL power profile measurement. The average full width at half maximum (FWHM) duration τ of the single-shot P_σ is 8.6 fs, with an rms shot-to-shot variation of 1.5 fs.

A systematic error term for τ is the time resolution, which leads to an overestimation of the FEL pulse duration. For the lasing part as in this power profile measurement (between approximately −10 and 5 fs), we assume an r_t around 2.5 fs [see Fig. 8(b)]. From the subtraction in quadrature of r_t from the measured values of τ (using a factor 2.335 to convert rms values to FWHM), we estimate a true FWHM bunch duration of 6.3 fs, meaning that r_t would have a relative impact of around 35%. In most measurements, we observe a much longer FEL pulse duration, in which case r_t only has negligible effect.

V. CONCLUSION

We presented time-resolved diagnostics at the European XFEL with a corrugated passive wakefield streaker. Compared to movable double-sided PS, our nonmovable single-sided PS has an even bigger advantage in cost-effectiveness over TDS diagnostics. We exploit the non-invasive CRISP diagnostics [37] for a reliable and consistent calibration of the beam trajectory.

To interpret the LPS measurements of the energy-chirped beam after the SASE2 beamline, we developed a slice energy resolution theory for electron streaking measurement setups, complementing an earlier study on the time resolution for PS diagnostics [30]. We find in simulations and measurements that the spillover of time into energy resolution is a major effect in our case. We showed LPS measurements with a time resolution down to few femtoseconds, and a slice energy resolution down to few MeV for time slices with small local energy chirp. We showed an example of FEL power profile measurement with an average FWHM photon pulse duration below 10 fs.

We also indicated which properties of the LPS our PS diagnostics cannot resolve. In particular, we cannot measure conclusively the mean slice energy of the beam tail, which we attribute to an insufficient understanding of the slice energy loss induced by the PS. We also cannot measure the slice energy spread of the nonlasing beam with sufficient resolution. For this purpose we suggest to employ the optical klystron effect instead [26,28].

The data and analysis software used for the results shown in this paper are available for download [43].

ACKNOWLEDGMENTS

APPENDIX A: SLICE ENERGY SPREAD INDUCED BY LONGITUDINAL WAKEFIELDS

In the wakefield model [34,35], the transverse effects are described by dipole (w_{yd}) and quadrupole (w_{yq}) wakefield components:

$$w_y(s, y) = w_{yd}(s) + y\, w_{yq}(s) \qquad (A1)$$

$$w_x(s, x) = -x\, w_{yq}(s), \qquad (A2)$$

and the longitudinal effect is described by w_l. All wakefield terms depend on the longitudinal distance s between drive and test particle. The quadrupole effect depends on the individual transverse test particle coordinates x and y relative to the beam centroid, while the other two effects do not. The energy spread increase imposed by the longitudinal wakefield component [44] is not explicitly calculated in Refs. [34,35], but we evaluate it here through the application of the Panofsky-Wenzel theorem [45]:

$$\frac{\partial}{\partial s} w_x = -\frac{\partial}{\partial x} w_l; \qquad \frac{\partial}{\partial s} w_y = -\frac{\partial}{\partial y} w_l, \qquad (A3)$$

where x and y refer to the transverse test particle coordinates, and s is the longitudinal coordinate (directed opposite the main direction of movement). The left-hand sides of the two equations above exist, whereas the available expressions for w_l have no x or y dependencies. Inserting Eqs. (A1) and (A2), we obtain one correction term from each w_{yd} and w_{yq}

$$-\int dy \frac{\partial}{\partial s} w_{yd} = -y\frac{\partial}{\partial s} w_{yd} \qquad (A4)$$

$$\int dx\, x \frac{\partial}{\partial s} w_{yq} - \int dy\, y \frac{\partial}{\partial s} w_{yq} = \frac{x^2 - y^2}{2} \frac{\partial}{\partial s} w_{yq}, \quad (A5)$$

which we use to define the corrected longitudinal wake function w_l^*:

$$w_l^* \equiv w_l - y\frac{\partial}{\partial s} w_{yd} + \frac{x^2 - y^2}{2} \frac{\partial}{\partial s} w_{yq}. \qquad (A6)$$

Next, we calculate the derivatives of w_{yd} and w_{yq} with respect to s. For each of these two functions, there exist two analytical expressions, one for the double-sided [34] and another for the single-sided [35] corrugated PS variant. Conveniently, all four expressions have the form

$$w(s) = A\left[1 - \left(1 + \sqrt{\frac{s}{s_0}}\right) \exp\left(-\sqrt{\frac{s}{s_0}}\right)\right], \qquad (A7)$$

with A and s_0 being functions of the corrugation geometry and the beam center of mass position inside the PS, and derivative

$$\frac{\partial w(s)}{\partial s} = \frac{A}{2s_0} \exp\left(-\sqrt{\frac{s}{s_0}}\right). \quad (A8)$$

The energy change of an individual particle in the bunch is given by a convolution with the beam longitudinal charge density $\rho(s)$:

$$\Delta E(s, x, y) = L \int_{-\infty}^{s} \mathrm{d}s' \rho(s') w_l^*(s - s', x, y)$$
$$\equiv L\left(W_l(s) - yW_{ld}(s) + \frac{x^2 - y^2}{2}W_{lq}(s)\right), \quad (A9)$$

where we denote W_{ld} and W_{lq} as the convolutions of the corresponding $\partial w_y/\partial s$ terms with $\rho(s)$, and where L is the length of the structure.

Assuming Gaussian transverse beam distributions characterized by σ_x and σ_y, we calculate the scaling of the induced energy spread with the beam sizes. We obtain the slice mean energy loss ΔE and rms energy spread increase $\Delta\sigma_E$ by integrating over the transverse beam distribution, as indicated by the angle brackets:

$$\Delta E(s) = \langle \Delta E(s, x, y) \rangle$$
$$= L\left(W_l(s) + W_{lq}(s)\frac{\sigma_x^2 - \sigma_y^2}{2}\right) \quad (A10)$$

$$\Delta\sigma_E^2(s) = \langle \Delta E^2(s, x, y) \rangle - \langle \Delta E(s, x, y) \rangle^2$$
$$= L^2\left(W_{ld}^2(s)\sigma_y^2 + W_{lq}^2(s)\frac{\sigma_x^4 + \sigma_y^4}{2}\right). \quad (A11)$$

For symmetry reasons, the slice mean energy change ΔE does not depend on W_{ld}: for every particle that receives an energy increase from the yW_{ld} term in Eq. (A9), there exists another particle with an opposite y coordinate that receives an energy decrease of the same magnitude. The quadrupole wakefield correction leads to an additional slice energy change if the beam is not round. Both the dipole and quadrupole wakefield corrections cause an energy spread increase. The simulated $\Delta\sigma_E$ in Fig. 4(d) is almost entirely from the W_{ld} correction term, with a negligible contribution from W_{lq}.

APPENDIX B: SLICE ENERGY RESOLUTION FOR AN INFINITELY LONG, FLAT BEAM

We analytically solve the time-resolved energy spread measurement of an infinitely long beam with constant beam current, constant energy chirp $h = \mathrm{d}\delta/\mathrm{d}t$, linear streaking

$\mu = \mathrm{d}y/\mathrm{d}t$, and linear dispersion $D = \mathrm{d}x/\mathrm{d}\delta$. The 4D density function at the screen, assuming Gaussian distributions in the natural coordinates x, y, and $\delta = (E - E_0)/E_0$, and without normalization factors, is

$$\rho_{4D} = \exp\left(-\frac{(x - D\delta)^2}{2\sigma_x^2} - \frac{(y - \mu t)^2}{2\sigma_y^2} - \frac{(\delta - ht)^2}{2\sigma_\delta^2}\right). \quad (B1)$$

A screen records the projection $\rho_{2D} = \int \mathrm{d}t \int \mathrm{d}\delta \rho_{4d}$. We evaluate the horizontal rms beam size σ_{xm} along the streaked (vertical) dimension:

$$\sigma_{xm}^2 = \frac{\int \mathrm{d}x\, x^2 \rho_{2D}(x, y)}{\int \mathrm{d}x\, \rho_{2D}(x, y)} - \left(\frac{\int \mathrm{d}x\, x\, \rho_{2D}(x, y)}{\int \mathrm{d}x\, \rho_{2D}(x, y)}\right)^2$$
$$= \sigma_x^2 + (D\sigma_\delta)^2 + \left(\frac{Dh\sigma_y}{\mu}\right)^2, \quad (B2)$$

and identify the measured energy spread σ_{Em} as $E_0\sigma_{xm}/D$. Attributing the difference between σ_{Em} and the true energy spread $E_0\sigma_\delta$ to resolution effects, we obtain the slice energy resolution

$$r_E^* = \sqrt{\left(\frac{E_0\sigma_x}{D}\right)^2 + \left(\frac{\sigma_y}{\mu}\frac{\mathrm{d}E}{\mathrm{d}t}\right)^2}, \quad (B3)$$

equal to Eq. (5) with $\Delta\sigma_E = 0$ and $r_t = \sigma_y/|\mu|$.

APPENDIX C: COMPARISON OF TRACKING CODES

For simulation results shown earlier in this paper, we use the particle tracking functionality of the custom PWFM code [29]. It implements the aforementioned analytical wakefield model [34], and also the longitudinal wakefield corrections given in Appendix A. The code treats the beam as rigid inside the PS and models the PS as a combination of a half-length drift, a point kick, and another half-length drift. Therefore, each wakefield potential needs to be only calculated once, which is advantageous in terms of tracking speed. However, once the wakefields become too strong, clearly, the rigid beam approximation is no longer accurate.

Here, we compare PWFM to the OCELOT code [42], which models a flat corrugated PS as many point kick sources interleaved by drift spaces and thus resolves the dynamics of the beam inside the corrugated structure. It implements the modal summation method for rectangular corrugated structures [46] and respects the Panofsky-Wenzel theorem on a fundamental level. It contains also a third transverse wakefield component, which is relevant for beams that are tilted inside the structure [47].

We generate a 6D particle distribution as described in Sec. III B. The initial beam has zero energy spread. The step size for OCELOT is set to 0.1 m. We use d values of 400, 500, and 600 μm to find the limit of PWFM's accuracy.
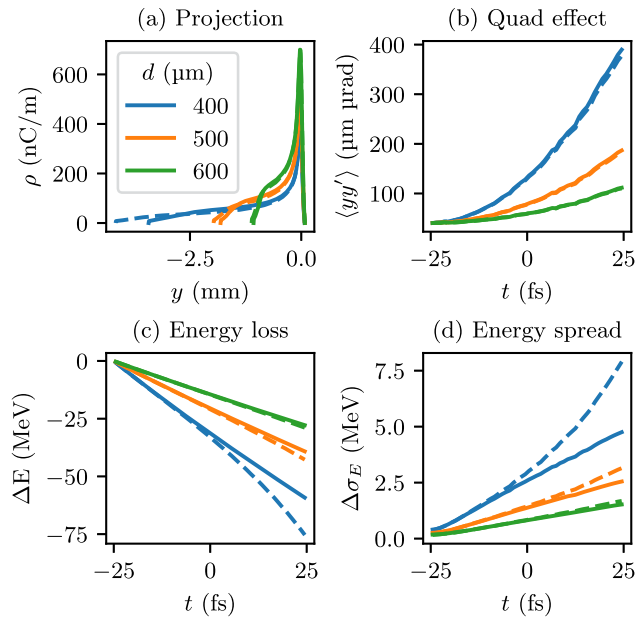
FIG. 10. Comparison of the PWFM (solid) and OCELOT codes (dashed) in tracking a particle distribution from the PS to the screen. (a) Simulated streaked transverse distribution at the screen. (b) Evaluation of the time-resolved transverse quadrupole effect in streaking direction. (c),(d) Slice energy loss and slice energy spread.

Figure 10 shows the analysis of the two tracking simulations. We compare the simulated transverse particle distribution at the screen in (a). The quadrupole effect increases the correlation between vertical positions and angles ($\langle yy' \rangle$). We evaluate this quantity directly after the wakefield effects are applied for different time slices and display the result in (b). A comparison of the wakefield-induced energy loss and energy spread is shown in plots (c), (d). There is generally excellent agreement between the two codes for $d = 600$ μm and $d = 500$ μm. We only see significant differences in the energy loss and energy spread at $d = 400$ μm and emphasize that all experiments shown earlier in this paper were performed with d larger than 500 μm.

[1] C. Pellegrini, A. Marinelli, and S. Reiche, The physics of x-ray free-electron lasers, Rev. Mod. Phys. 88, 015006 (2016).

[2] N. Huang, H. Deng, B. Liu, D. Wang, and Z. Zhao, Features and futures of X-ray free-electron lasers, Innovation 2, 100097 (2021).

[3] S. Tomin, J. Kaiser, N. Maris Lockmann, T. Wohlenberg, and I. Zagorodnov, Undulator linear taper control at the European X-Ray Free-Electron Laser facility, Phys. Rev. Accel. Beams 27, 042801 (2024).

[4] A. Fadini, S. Reiche, K. Nass, and J. J. van Thor, Applications and limits of time-to-energy mapping of

protein crystal diffraction using energy-chirped polychromatic XFEL pulses, Appl. Sci. 10, 2599 (2020).

[5] K. Nass, C. Bacellar, C. Cirelli, F. Dworkowski, Y. Gevorkov, D. James, P. J. M. Johnson, D. Kekilli, G. Knopp, I. Martiel et al., Pink-beam serial femtosecond crystallography for accurate structure-factor determination at an X-ray free-electron laser, Int. Union Crystallogr. J. 8, 905 (2021).

[6] A. M. Kondratenko and E. L. Saldin, Generation of coherent radiation by a relativistic electron beam in an undulator, Part. Accel. 10, 207 (1980).

[7] R. Bonifacio, C. Pellegrini, and L. M. Narducci, Collective instabilities and high-gain regime in a free electron laser, Opt. Commun. 50, 373 (1984).

[8] E. L. Saldin, E. A. Schneidmiller, and M. V. Yurkov, Longitudinal space charge-driven microbunching instability in the TESLA Test Facility linac, Nucl. Instrum. Methods Phys. Res., Sect. A 528, 355 (2004).

[9] Y. Ding, C. Behrens, P. Emma, J. Frisch, Z. Huang, H. Loos, P. Krejcik, and M.-H. Wang, Femtosecond X-ray pulse temporal characterization in free-electron lasers using a transverse deflector, Phys. Rev. ST Accel. Beams 14, 120701 (2011).

[10] C. Behrens, F.-J. Decker, Y. Ding, V. A. Dolgashev, J. Frisch, Z. Huang, P. Krejcik, H. Loos, A. Lutman, T. J. Maxwell et al., Few-femtosecond time-resolved measurements of X-ray free-electron lasers, Nat. Commun. 5, 3762 (2014).

[11] P. Dijkstal, A. Malyzhenkov, P. Craievich, E. Ferrari, R. Ganter, S. Reiche, T. Schietinger, P. Juranić, and E. Prat, Self-synchronized and cost-effective time-resolved measurements at X-ray free-electron lasers with femtosecond resolution, Phys. Rev. Res. 4, 013017 (2022).

[12] H. N. Chapman, C. Caleman, and N. Timneanu, Diffraction before destruction, Phil. Trans. R. Soc. B 369, 20130313 (2014).

[13] L. Young, K. Ueda, M. Gühr, P. H. Bucksbaum, M. Simon, S. Mukamel, N. Rohringer, K. C. Prince, C. Masciovecchio, M. Meyer et al., Roadmap of ultrafast X-ray atomic and molecular physics, J. Phys. B 51, 032003 (2018).

[14] H. N. Chapman, X-ray free-electron lasers for the structure and dynamics of macromolecules, Annu. Rev. Biochem. 88, 35 (2019).

[15] P. Emma, J. Frisch, and P. Krejcik, A transverse rf deflecting structure for bunch length and phase space diagnostics, Stanford Linear Accelerator Center, LCLS Report No. LCLS-TN-00-12, 2000.

[16] K. Floettmann and V. V. Paramonov, Beam dynamics in transverse deflecting rf structures, Phys. Rev. ST Accel. Beams 17, 024001 (2014).

[17] C. Wiebers, M. Holz, G. Kube, D. Nölle, G. Priebe, and H.-C. Schröder, Scintillating screen monitors for transverse electron beam profile diagnostics at the European XFEL, in Proceedings of the 2nd International Beam Instrumentation Conference, IBIC 2013, Oxford, United Kingdom, edited by I. Martin and G. Rehm (JACoW, Geneva, Switzerland, 2013), WEPF03.

[18] S. Bettoni, P. Craievich, A. A. Lutman, and M. Pedrozzi, Temporal profile measurements of relativistic electron

bunch based on wakefield generation, Phys. Rev. Accel. Beams 19, 021304 (2016).

[19] J. Seok, M. Chung, H.-S. Kang, C.-K. Min, and D. Na, Use of a corrugated beam pipe as a passive deflector for bunch length measurements, Phys. Rev. Accel. Beams 21, 022801 (2018).

[20] S. Tomin, W. Decking, N. Golubeva, A. Novokshonov, T. Wohlenberg, and I. Zagorodnov, Longitudinal phase space diagnostics with corrugated structure at the European XFEL, in *Proceedings of the 13th 1International Particle Accelerator Conference, IPAC 2022, Bangkok, Thailand*, edited by F. Zimmermann, H. Tanaka, P. Sudmuang, P. Klysubun, P. Sunwong, T. Chanwattana, C. Petit-Jean-Genaz, and V. R. W. Schaa (JACoW, Geneva, Switzerland, 2022), MOPOPT020.

[21] E. Prat, R. Abela, M. Aiba, A. Alarcon, J. Alex, Y. Arbelo, C. Arrell, V. Arsov, C. Bacellar, C. Beard *et al.*, A compact and cost-effective hard X-ray free-electron laser driven by a high-brightness and low-energy electron beam, Nat. Photonics 14, 748 (2020).

[22] W. Decking, S. Abeghyan, P. Abramian, A. Abramsky, A. Aguirre, C. Albrecht, P. Alou, M. Altarelli, P. Altmann, K. Amyan *et al.*, A MHz-repetition-rate hard X-ray free-electron laser driven by a superconducting linear accelerator, Nat. Photonics 14, 391 (2020).

[23] A. Novokhatski, Wakefield potentials of corrugated structures, Phys. Rev. ST Accel. Beams 18, 104402 (2015).

[24] S. Huang, Y. Ding, Y. Feng, E. Hemsing, Z. Huang, J. Krzywinski, A. A. Lutman, A. Marinelli, T. J. Maxwell, and D. Zhu, Generating single-spike hard x-ray pulses with nonlinear bunch compression in free-electron lasers, Phys. Rev. Lett. 119, 154801 (2017).

[25] A. Trebushinin, G. Geloni, S. Serkez, G. Mercurio, N. Gerasimova, T. Maltezopoulos, M. Guetg, and E. Schneidmiller, Experimental demonstration of attoseconds-at-harmonics at the SASE3 undulator of the European XFEL, Photonics 10, 131 (2023).

[26] G. Penco, E. Allaria, G. De Ninno, E. Ferrari, L. Giannessi, E. Roussel, and S. Spampinati, Optical klystron enhancement to self amplified spontaneous emission at FERMI, Photonics 4, 15 (2017).

[27] E. Allaria, D. Castronovo, P. Cinquegrana, P. Craievich, M. Dal Forno, M. B. Danailov, G. D'Auria, A. Demidovich, G. De Ninno, S. Di Mitri *et al.*, Highly coherent and stable pulses from the FERMI seeded free-electron laser in the extreme ultraviolet, Nat. Photonics 6, 699 (2012).

[28] E. Prat, C. Kittel, M. Calvi, P. Craievich, P. Dijkstal, S. Reiche, T. Schietinger, and G. Wang, Experimental characterization of the optical klystron effect to measure the intrinsic energy spread of high-brightness electron beams, Phys. Rev. Accel. Beams 27, 030701 (2024).

[29] P. Dijkstal, Temporal FEL pulse shaping and diagnostics at SwissFEL, Ph.D. thesis, ETH Zurich, 2022.

[30] P. Craievich and A. A. Lutman, Effects of the quadrupole wakefields in a passive streaker, Nucl. Instrum. Methods Phys. Res., Sect. A 865, 55 (2017).

[31] P. Dijkstal, R. Ganter, P. Heimgartner, A. Malyzhenkov, E. Prat, S. Reiche, and P. Craievich, Corrugated wakefield structures at SwissFEL, in *Proceedings of 14th International Particle Accelerator Conference, IPAC-2023, Venice, Italy*, edited by R. Assmann, P. McIntosh, G. Bisoffi, A. Fabris, I. Andrian, and G. Vinicola (JACoW, Geneva, Switzerland, 2023), THPL153.

[32] J. Han, J. Hong, J. Lee, M. Chae, S. Baek, H. Choi, T. Ha, J. Hu, W. Hwang, S. Jung *et al.*, Beam operation of the PAL-XFEL injector test facility, in *Proceedings of FEL2014, Basel, Switzerland*, edited by J. Chrin, S. Reiche, and V. R. W. Schaa (JACoW, Geneva, Switzerland, 2015), WEB02.

[33] S. Tomin, E. Schneidmiller, and W. Decking, First measurement of energy diffusion in an electron beam due to quantum fluctuations in the undulator radiation, Sci. Rep. 13, 1605 (2023).

[34] K. Bane, G. Stupakov, and I. Zagorodnov, Analytical formulas for short bunch wakes in a flat dechirper, Phys. Rev. Accel. Beams 19, 084401 (2016).

[35] K. Bane, G. Stupakov, and I. Zagorodnov, Wakefields of a beam near a single plate in a flat dechirper, Stanford Linear Accelerator Center Report No. SLAC-PUB 16881, 2016.

[36] S. Meykopff and B. Beutner, Emittance measurement and optics matching at the European XFEL, in *Proceedings of the 16th International Conference on Accelerator and Large Experimental Control Systems, ICALEPCS 2017, Barcelona, Spain*, edited by I. Costa, D. Fernánedz, Ó. Matilla, and V. R. W. Schaa (JACoW, Geneva, Switzerland, 2018), THPHA116.

[37] N. M. Lockmann, C. Gerth, B. Schmidt, and S. Wesch, Noninvasive THz spectroscopy for bunch current profile reconstructions at MHz repetition rates, Phys. Rev. Accel. Beams 23, 112801 (2020).

[38] T. Maltezopoulos, F. Dietrich, W. Freund, U. F. Jastrow, A. Koch, J. Laksman, J. Liu, M. Planas, A. A. Sorokin, K. Tiedtke *et al.*, Operation of X-ray gas monitors at the European XFEL, J. Synchrotron Radiat. 26, 1045 (2019).

[39] W. Qin, Y. Ding, A. A. Lutman, and Y.-C. Chao, Matching-based fresh-slice method for generating two-color X-ray free-electron lasers, Phys. Rev. Accel. Beams 20, 090701 (2017).

[40] D. Ratner, C. Behrens, Y. Ding, Z. Huang, A. Marinelli, T. Maxwell, and F. Zhou, Time-resolved imaging of the microbunching instability and energy spread at the Linac Coherent Light Source, Phys. Rev. ST Accel. Beams 18, 030704 (2015).

[41] E. Prat, P. Dijkstal, E. Ferrari, A. Malyzhenkov, and S. Reiche, High-resolution dispersion-based measurement of the electron beam energy spread, Phys. Rev. Accel. Beams 23, 090701 (2020).

[42] I. Agapov, G. Geloni, S. Tomin, and I. Zagorodnov, OCELOT: A software framework for synchrotron light source and FEL studies, Nucl. Instrum. Methods Phys. Res., Sect. A 768, 151 (2014).

[43] P. Dijkstal, Longitudinal phase space diagnostics with a non-movable corrugated passive wakefield streaker, 10.5281/zenodo.10673910 (2024).

[44] K. Bane and G. Stupakov, Dechirper wakefields for short bunches, Nucl. Instrum. Methods Phys. Res., Sect. A 820, 156 (2016).

[45] M. Dohlus and R. Wanzenberg, An introduction to wake fields and impedances, in *Proceedings of the CAS-CERN Accelerator School on Intensity Limitations in Particle Beams*, edited by W. Herr (CERN, Switzerland, 2017), Vol. 3.

[46] I. Zagorodnov, G. Feng, and T. Limberg, Corrugated structure insertion for extending the SASE bandwidth up to 3% at the European XFEL, Nucl. Instrum. Methods Phys. Res., Sect. A **837**, 69 (2016).

[47] W. Qin, M. Dohlus, and I. Zagorodnov, Short-range wakefields in an L-shaped corrugated structure, Phys. Rev. Accel. Beams **26**, 064402 (2023).